Article

Numerical Prediction on the Dynamic Response of a Helical Floating Vertical Axis Wind Turbine Based on an Aero-Hydro-Mooring-Control Coupled Model

Yan Li [1,2], Liqin Liu [1,2,*], Ying Guo [1,2,3,*] and Wanru Deng [1,2]

1   State Key Laboratory of Hydraulic Engineering Simulation and Safety, School of Civil Engineering, Tianjin University, Tianjin 300354, China; liyan_0323@tju.edu.cn (Y.L.); dengwanru@tju.edu.cn (W.D.)
2   Tianjin Key Laboratory of Port and Ocean Engineering, School of Civil Engineering, Tianjin University, Tianjin 300354, China
3   Tianjin Navigation Instrument Research Institute, Tianjin 300131, China
*   Correspondence: liuliqin@tju.edu.cn (L.L.); yynocry@tju.edu.cn (Y.G.)

Abstract: Considering the aero-hydro-mooring-control coupled performance of a floating Vertical Axis Wind Turbine (VAWT), the numerical model of the floating helical VAWT system is established, and the fully coupled simulation program of the floating helical VAWT is developed. The aerodynamic load of the wind turbine system is calculated using the unsteady BEM model, and the hydrodynamic load is calculated using the 3D potential theory. The floating foundation is considered as a rigid body, and the blades and tower are considered as flexible bodies. Based on the Kane method of a multi-body system, the dynamic responses of the VAWT could be solved in the time domain. A variable speed control model considering efficiency and load is established to match the rotating speed with the wind speed, and it could maintain the target output power under the influence of turbulent wind and large-scale movement of the floating foundation. The control strategy of limiting the target speed change rate and low-pass filtering is adopted to ensure the rapid regulation of the wind turbine under low wind speed conditions and stable regulation under high wind speed conditions.

Keywords: vertical axis wind turbine; semi-submersible foundation; control strategy; hydrodynamics; aerodynamics; second order wave forces

1. Introduction

Due to the worldwide energy shortage and low carbon emission requirement, renewable energies have obviously been promoted in recent decades. According to the Global Wind Energy Council (GWEC), the worldwide installation capacity of wind turbines in 2020 is 93.0 GW, which increased by 53% compared to 2019 [1]. However, it should be realized that only 6.5% of the newly installed turbines are the offshore ones. In other words, there are still many difficulties and challenges in offshore wind farm development. Another critical challenge is the potential resources. In the past, many offshore wind turbines have been established in shallow water areas near the coastal line. This high-speed expansion leads to the issues that the remaining wind resources and available areas decrease in the coastal areas. On the contrary, the wind conditions are much better in the deep-water zone, such as greater wind speed, less shelter, lower turbulence, etc. Hereby, it is an unstoppable trend to develop offshore wind farms in the deep-water areas.

When the water depth is greater than 50 m, it is usually recognized that the cost and difficulties of the wind turbine installation, operation, and maintenance will be exponentially increased. The mature technology of the fixed offshore wind turbines cannot be adopted in deep-water areas, so the floating offshore wind turbine (FOWT) becomes an important solution. The major buoy types are based on the experience of offshore oil and gas platforms, and these are the SPAR, semi-submersible, barge, and TLP, etc. [2].

On the other hand, due to the different rotating axis, wind turbines could be divided into two major kinds, which are the horizontal axis wind turbines (HAWTs) and the VAWTs [3]. Comparing with the VAWTs, the HAWTs have rapidly developed in the past 30 decades, and they have occupied most of the wind turbine market. It is commonly recognized that the capacity of a HAWT has a linear relationship with the rotor plane area. Therefore, longer blades, higher towers, and heavier rotors will be undoubtedly needed for the larger-capacity HAWTs, and it may cause potential risks, such as uncertain motion and larger inertia loads. To overcome these shortcomings of HAWTs, vertical rotors are proposed. The most significant improvement in the VAWT is that the rotor and blade structures could be simplified and the nacelle could be arranged at the bottom of the rotor, which makes the installation and maintenance works easier [4,5]. Another advantage of VAWTs is the rotation axis being perpendicular to both incident wind and the free sea surface. With the assistance of the vertical axis, the rotor is not sensitive to the inflow wind direction, and the yaw control system on the HAWTs could be removed to lighten the structure weight. From this aspect, the use of VAWTs can be much easier in terms of increasing the capacity and has more benefits for large-capacity wind turbines [6–9].

However, the VAWTs also have several disadvantages. On one hand, the aerodynamic performance and the efficiency of VAWTs is much lower than HAWTs [10]. The time varying blade azimuth and the changing attack angle will make the flow field more complicated. On the other hand, the VAWTs, especially the traditional ones, cannot start themselves under low wind velocity conditions. Particularly, the rotor speed is relatively difficult to control and limit. Moreover, the long-term power generation progress may lead to issues on the blades, including fatigue, cracking, or even fracture. To overcome these problems, many successful attempts have been undertaken to improve the aerodynamic performance of the straight blade [11]. Another possible improvement is to change the straight blade into a helical shape. It is confirmed that both the aerodynamic performance and the structural responses could be ameliorated, to improve the robustness of the power generation [12,13]. According to the previous investigations [14,15], an optimization study is undertaken to determine a better helical twist angle of the blade, and its performance is validated using a reasonable mathematical model.

A common approach for investigating the dynamic performance of FOWTs is to adopt the code to conduct the numerical simulations. During the past decade, some commercial software, for example, FAST, BLADED, SIMA, etc., was released and widely used in the works of FOWT dynamic behavior prediction. However, most of these commercial packages always focus on the HAWTs, which are more successfully commercialized than the offshore VAWTs. However, some in-house CAE tools have been gradually developed to execute the numerical simulations on the VAWTs. Wang et al. [16,17] took the changing Reynold number and the dynamic stall effect into consideration. They calculated the aerodynamic loads using the double-disk multiple-stream-tube (DMST) model and developed the numerical tool SIMO-RIFLEX-DMS to perform the simulations on the floating VAWTs. Based on these works, Cheng et al. [18,19] further improved the aerodynamics algorithm by adopting the actuator cylinder theory. According to the results, they found that the blade number has a significant influence on the tower base moment but has little effect on power generation and other dynamic responses. Another widely known in-house code FloVAWT was developed by Collu et al. [20]. The DMST model and the potential theory were adopted in this code to investigate the motions of floating VAWTs. Because the blades and tower are modeled as a rigid body, the code could be used in the primary design stage of the VAWTs. Therefore, Borg et al. [21,22] used it to calculate the motions of different VAWTs which consist of the 5MW Darrieus-type rotor and different support buoys, and their results show that the buoy motion has an infinitesimal influence on the maximum aerodynamic loads. Owens et al. [23,24] investigated the structural vibration and buoy motion stability of a large floating VAWT, based on their in-house rigid–flexible coupled simulation tool. The coupled effect between the modes of the blade and tower is obvious. Specifically, the tower vibration frequency is influenced by the rotation speed, which causes the outstanding local

resonance. Vita et al. [25] improved HAWC2 by adding some Dynamic Link Libraries to realize the aerodynamic calculations of the VAWTs. Based on this new function, they performed a couple of simulations on the dynamic behaviors of a SPAR-type VAWT. Based on multi-body kinematics and the rigid–flexible coupled algorithm, Deng et al. [26] investigated the dynamic responses of an H-type floating VAWT using an in-house code. Both buoy motion and vibrations of the slender systems were calculated under wind, waves, and currents. GAO et al. [27] proposed a half-coupled aero-hydro-control simulation model. Taking the rotor rotation as a separate degree of freedom (DOF), a seven-DOF motion governing equation was established for a TLP-type VAWT. Their simulation results were also validated by Orcaflex. Tan and Ikoma et al. [28,29] investigated a four-moonpool barge type VAWT numerically and experimentally. According to their study, its robust hydrodynamic performance was validated and the second order mean drift force was reasonably shown. Moreover, there are several experiments that study the features of FOWTs, but most of the models are HAWTs and little attention was paid to the VAWTs [6,30,31].

Another key mechanism of VAWT is the controlling strategy to release the loads on the blades. This is important to ensure the safety of the floating system. The PID controllers are most commonly used for the floating HAWTs. To be specific, the rotor speed is adjusted when the wind velocity is lower than the rated speed, while the blade pitch angle is increased under the high wind speed cases. However, for those bending blades on the VAWTs, such as Darrieus type and helical type, we cannot change their pitch angles because the twist angles are finalized once it is manufactured. Therefore, the pitch angle controlling strategies are seldom available on these VAWTs, and it is essential to develop a robust rotor speed controlling algorithm. To achieve this goal, Svendsen et al. [32,33] provided a targeted PID-based speed controller for a Darrieus-type 5MW VAWT. According to the experimental investigation, they validated the effectiveness of the controller and checked the sensitivities of the PID parameters. Compared with the HAWT controllers, the controlling targets for the VAWT are the optimized speed corresponding to the max power generation and the rotor speed under the cases of both low and high wind speeds, respectively. Cheng et al. [34] further improved this controlling algorithm. Their controlling target for the rotor speed under the high wind speed cases was the corresponding speed to the rated output power. According to the simulation results, the aerodynamic performance and the mooring system show prominent 2P variation.

To investigate the dynamic behavior of VAWTs, the key mechanisms include: the wave–body interaction hydrodynamic loads on the floating buoy, the nonlinear restoring mooring force in the mooring lines, the unsteady aerodynamic effects on the blades, and the corresponding rotor controlling strategy. In our following study, an aero-hydro-mooring-control coupled simulation model is established for a semi-helical VAWT. Therefore, we applied an in-house code HeVAWT which is composed of a hydrodynamic module based on the 3D potential theory, an aerodynamic module based on the 2D unsteady blade element momentum (BEM) theory, a quasi-static catenary mooring module, and a PID-based rotor speed control module. After adopting these algorithms in the time domain, the numerical model can simulate nonlinear dynamic responses of VAWT in different scenarios. In the following works, an optimized 5MW floating helical VAWT is adopted, and both the dynamic behaviors and the controlling effect are studied numerically.

In the following section, the configuration as well as physical parameters of the helical VAWT are described. Then, brief clarifications of the numerical models are displayed, including the coupled dynamic simulation model and the controlling strategy. This is followed by the code validation with experimental results. The numerical results, including predictions of dynamic responses under different scenarios are then presented. Finally, conclusions are drawn.

2. Physical Problem Description

According to the configuration in Figure 1, the floating VAWT system in the following simulations consists of the semi-type floater and a 5MW VAWT. To be specific, the VAWT is an optimized 5 MW helical wind turbine [35] (see Table 1), while the floating buoy uses the OC4 DeepCWind floater (see Figure 2). The mooring system consists of three uniformly distributed mooring lines [36] (see Tables 2 and 3). Specifically, Line #2 is located in the 0 deg direction. In other words, it is along the inflow wind and wave directions. A Cartesian coordinate system is defined to show the buoy motion. The free surface is located at the z = 0 plane.

Table 1. Parameters of the wind turbine.

Items	Value
Rated power (MW)	5.3
Number of the blade	3
Rated rotation speed (rad/s)	1.08
Rated wind speed (m/s)	14.0
Cut in wind speed (m/s)	5.0
Cut out wind speed (m/s)	25.0
Total tower height above sea level (m)	80
Blade clear height (m)	84
Blade horizontal max diameter (m)	76.4
Blade mass (kg)	84,750
Tower mass (kg)	343,683.5
Blade section airfoil	NACA0018

Table 2. Parameters of the DeepCWind floating foundation.

Items	Value
Draft (m)	20.0
Distance between the columns (m)	50.0
Diameter of the columns (m)	12.0
Height of the columns (m)	26.0
Diameter of the ballast tank (m)	24.0
Height of the ballast tank (m)	6.0
Diameter of the central column (m)	6.5
Diameter of the truss (m)	1.6
Displacement (ton)	1411.4

Table 3. Parameters of mooring lines.

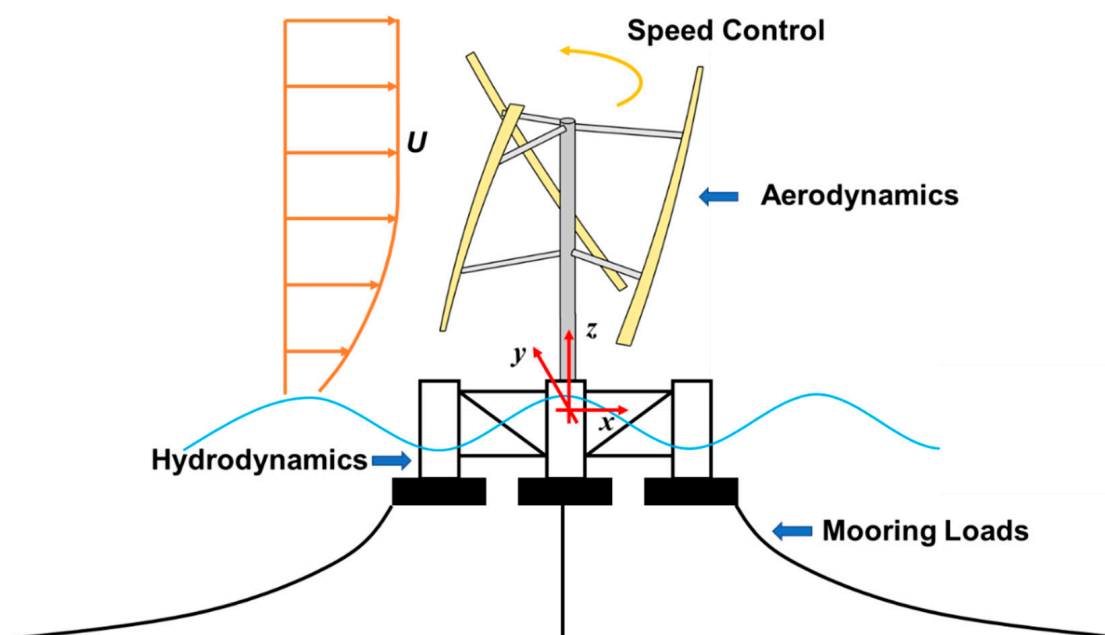| Items	Value
Depth to anchors below SWL (water depth)	200
Depth to fairleads below the SWL	14
Radius to anchors from the platform centerline	837.6
Radius to fairleads from the platform centerline	40.87
Mass in air (kg/m)	108.63
Extensional stiffness (N)	7.54×10^8
Diameter (mm)	76.6
Length (m)	835.5

Figure 1. Definition of the physical problem.
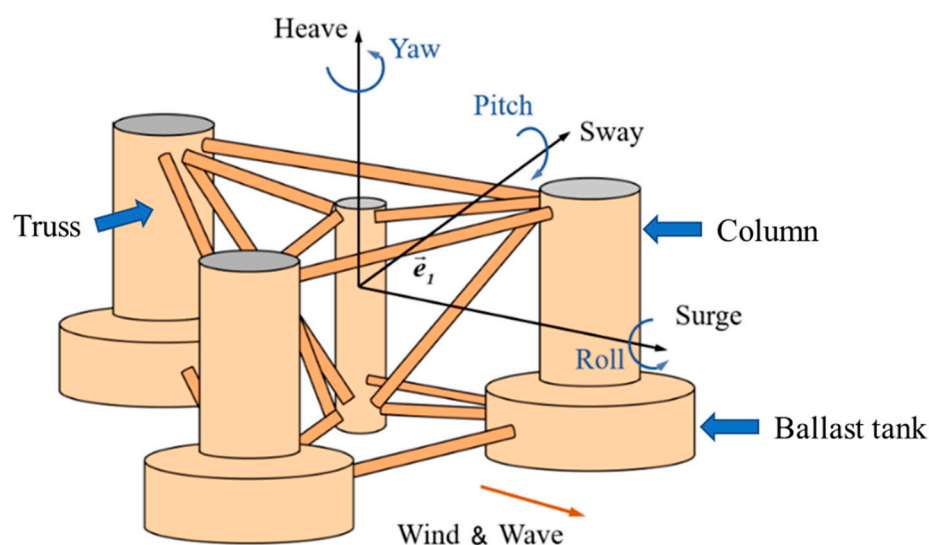

**Figure 2.** Definition of the DOFs of the floater.

3. Methodology

3.1. Aerodynamic Loads

The original BEM algorithm is the most commonly used numerical approach for calculating the aerodynamic load of the HAWTs [37]. Although it is a quasi-static model, the efficiency and accuracy of this algorithm has been approved in the previous studies on both fixed and floating offshore HAWTs. However, due to the different rotating axis, the classic BEM method cannot be used in the aerodynamic performance prediction of VAWTs. The DMST algorithm, hereby, is proposed to solve this problem, but it is only effective under the condition of limited sharp speed ratio. When the sharp speed ratio exceeds a specific range, divergence easily occurs, resulting in inaccurate calculation results. Taking the retardation effect caused by the dynamic inflow and wake into consideration, the 2D unsteady BEM algorithm [38], which is improved by the classic BEM approach, is adopted for the helical VAWT. Although the azimuths of the blades are time-varying, the factors could be converged in the time-domain simulation. Therefore, the iteration progress is not necessary in each time step, and the CPU-time could be saved.

The helical-type rotor could be recognized as a special kind of H-type VAWT, as shown in Figure 3. After dividing the straight blade into several parts, the torsion angles could be added on each element, so that the central line could achieve the helical curve. From this aspect, we could calculate the aerodynamic loads on the blades using an improved DMST algorithm. Specifically, by taking the difference angle between each blade part into consideration, the general wind loads on the rotor could be integrated along the twist blades. The local helical twist angle could be expressed as,

$$\psi = \frac{1}{2}\psi_0\zeta,$$ (1)

where ψ_0 is the general twist angle of the helical blade, $\zeta = \frac{z}{H}$ is the distance from the equator plane to the stream tube. To be specific, the helical angle corresponding to the equator plane is assumed as zero.
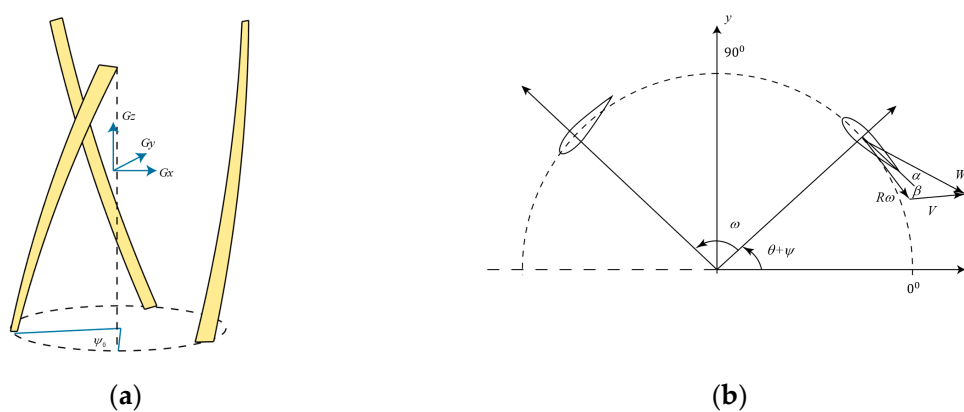
Figure 3. Schematic of the flow angles of a VAWT with helical blades. (**a**) side view; (**b**) top view.

3.2. Hydrodynamic Loads

For the diffraction and radiation effect, the wave loads on the floaters are simulated by the 3D potential theory. Assuming that the ideal flow field is nonrotatable, the potential term could be divided into three parts, which are incident term, diffraction term, and radiation term, respectively. All these three terms should follow the Laplace equation and the boundary conditions, including buoy surface, seafloor, free wave, and infinity. In the present work, the Airy wave is adopted to solve this boundary problem, and the wave loads could be achieved by integrating the wave pressure on the wet surface of the floater. Specifically, like other moored floating structures, the natural periods of the horizontal motions of the floating VAWT are in the range of low frequency and the resonant motion might be excited by the higher-order wave load. Therefore, the second-order difference–frequency wave loads are calculated by the full-QTF approach and they are considered in the time-domain simulations. On the other hand, because the semi-submersible buoy consists of the relative large-volume columns and the slender trusses, the Morison equation is also adopted to calculate the wave loads on the slender bodies, apart from the 3D potential theory. More details about the wave–body interaction could be observed in previous publications [39,40].

3.3. Mooring Tensions

As one of the essential parts on the FOWT system, the mooring tension has a significant influence on the dynamic behavior of the floating structure. Generally, there are many algorithms used to solve the response problem of this slender structure, such as the catenary model, lumped mass model, finite element model, etc. On one hand, although the catenary model is based on the quasi-static algorithm, it is widely used in the commercial codes because of its efficiency. However, the inertia effect and damping effect are not included in the catenary model. To overcome this issue, on the other hand, the dynamic models, such

as cable, bar, or beam, etc., are established to more accurately simulate the dynamic features of the mooring lines. Nevertheless, the dynamic algorithms still have some disadvantages, for example, time and memory costs, input coefficient determination, etc. Therefore, the main focus in the present work is the controlling strategy, the catenary module, which is more time saving than the finite element module. More details about these mooring modules could also be observed in our publications [41,42].

3.4. PID-Based Controller

Variable rotor speed control is a method used to adjust the rotor speed by controlling the generator torque. This method has been widely used and validated on HAWTs. It is also the most commonly used method to control the VAWTs with curved blades which cannot be adjusted by changing the blade pitch angle.

The diagram of the controller can be observed in Figure 4. In the control system, low-pass filtering is performed on the real-time input rotor speed ω_k at each moment to obtain $\omega_{k_{in}}$. Considering the influence of turbulence, floating foundation movement, and other factors on the incoming wind speed of the wind turbine, low-pass filtering was similarly carried out for real-time wind speed V, and the target rotor speed ω_{ref} was obtained according to the relationship between the wind speed and rotor speed. The relationship is as follows:

$$\omega_{ref} = \begin{cases} \omega_{opt}(\hat{V}), & \hat{V} < V_{rated} \\ \omega_{rate}, & V_{\Omega rated} \leq \hat{V} < V_{rated} \\ \omega_g(\hat{V}), & V_{rated} \leq \hat{V} \end{cases}, \tag{2}$$
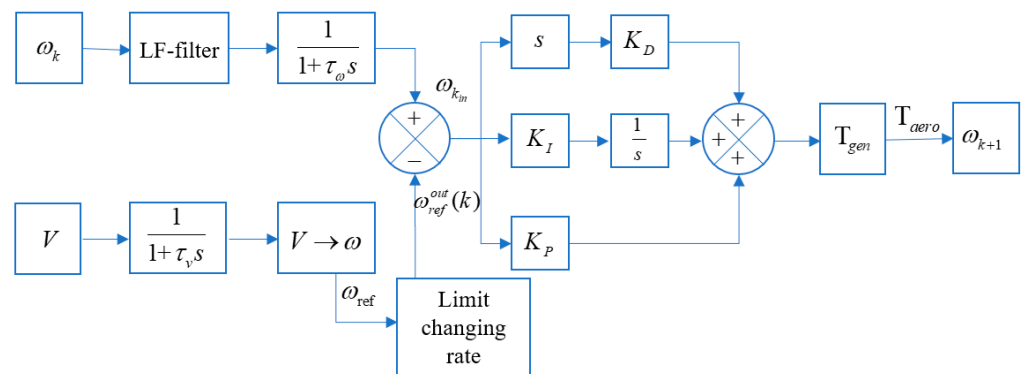

Figure 4. PID-based controller diagram of the helical VAWT.

In the equations above, $\hat{V}$ is the real-time relative incoming wind speed after low-pass filtering; $V_{\Omega rated}$ is the wind speed when the optimal speed reaches the rated speed if the wind speed is lower than the rated wind speed; $\omega_{opt}(\hat{V})$ is the rotor speed corresponding to the optimal TSR when the wind speed was $\hat{V}$; ω_{rate} is the rated speed; $\omega_{g(V)}$ is the speed corresponding to the rated power when the wind speed $\hat{V}$ is greater than the rated speed.

The difference between the real-time speed and the target speed at each moment is

$$\Delta\omega_k = \omega_{k_{in}} - \omega_{ref}, \tag{3}$$

The operational wind speed for the helical VAWT is in the range from 5 to 25 m/s, which is a relatively large band. On one hand, when the wind speed is low, the target speed changes fast with the wind speed. To guarantee that the wind turbine can operate at the optimal TSR, it is necessary to use a small time constant to filter the actual wind speed, so as to avoid that the target speed cannot match the change in real-time wind speed due to the large filtering time constant. When the wind speed is high, the target speed slows down with the change in wind speed, and the load of the wind turbine changes dramatically, which requires a large filter time constant. If a small time constant is still used to filter the

real-time wind speed, control overflow would occur, which will further increase the load fluctuation, and even lead to system instability and wind turbine structure damage. In fact, it is difficult to satisfy the control requirements of wind turbines under low wind speed and high wind speed at the same time using a single filter time constant. Therefore, the concept of change rate of target speed is introduced to limit the change in target speed when the wind speed is high, so that the wind turbine will not cause a large fluctuation in load when using a small time constant filter.

The target speed change rate is limited by the regulating ability of the generator (control system), so it should be ensured that the target speed change rate does not exceed the adjustable range of the generator. According to the wind speed after low-pass filtering, the target speed $\omega_{ref}^{in}(k)$ can be obtained by interpolation calculation. Through Equation (4), the target speed $\omega_{ref}^{out}(k)$ can be obtained considering the modification of the target speed change rate,

$$\omega_{ref}^{out}(k) = \begin{cases} \omega_{ref}^{out}(k-1) + U, & \omega_{ref}^{in}(k) - \omega_{ref}^{out}(k-1) > U \\ \omega_{ref}^{in}(k) & L \leq \omega_{ref}^{in}(k) - \omega_{ref}^{out}(k-1) \leq U \\ \omega_{ref}^{out}(k-1) + L, & \omega_{ref}^{in}(k) - \omega_{ref}^{out}(k-1) < L \end{cases} , \qquad (4)$$

where in and out represent before and after the rate of change is processed, respectively. U and L represent, respectively, the upper and lower bounds of the change in target speed. The values of U and L should satisfy the following inequalities:

$$\begin{cases} L \geq \int_{t_{k-1}}^{t_k} \frac{T_{aero}(\tau) - T_{gen,\max}}{J} d\tau \\ U \leq \int_{t_{k-1}}^{t_k} \frac{T_{aero}(\tau) - T_{gen,\min}}{J} d\tau \end{cases} , \qquad (5)$$

According to the above control strategy, the control system achieves the purpose of controlling the speed of the wind turbine by providing the regulation of torque, so that it is consistent with the target speed as much as possible. The regulating torque ΔT can be calculated from Equation (6),

$$\Delta T(t) = K_P \Delta \omega(t) + K_I \int_0^t \Delta \omega(\tau) d\tau + K_D \frac{d}{dt} \Delta \omega(t), \qquad (6)$$

where K_P, K_I, and K_D are the proportional, integral, and differential gain coefficients of the PID controller, respectively.

The regulating torque calculated by Equation (6) is an ideal result, without considering the limitation of the regulating capacity of the generator. In fact, the regulating torque of the wind turbine should be within the capacity of the generator and not exceed the maximum torque of the generator. In addition, due to the inherent protection mechanism of the generator, it takes a certain amount of time to increase or decrease the torque, and the target torque cannot be reached instantaneously.

The generator torque should be within the range that the generator can provide, and should also meet the requirements of the maximum reaction speed, such as:

$$T_{gen}^{\min} \leq T_{gen} \leq T_{gen}^{\max}, \qquad (7)$$

$$\dot{T}_{gen} \leq V_{T_{gen}}^{\max}, \qquad (8)$$

where the minimum generator torque $T_{gen}^{\min}$ equals zero and $T_{gen}^{\max}$ denotes the maximum torque that the generator can provide. The maximum reaction speed of the generator is $V_{T_{gen}}^{\max} = T_{gen}^{\max}/\tau_0$ and τ_0 is the time required for the generator to increase the torque from

zero to the maximum torque. The rotational speed at the next moment can be obtained through Equation (9), i.e.,

$$\omega_{k+1} = \frac{\Delta T}{J_{rotor} + J_{gen}} \Delta t + \omega_k, \tag{9}$$

where ω_k is the rotational speed of the wind turbine without low-pass filtering at the current time, J_{rotor} is the inertia of the wind turbine (including tower, brace, etc.), and J_{gen} is the moment of inertia of the generator.

3.5. Aero-Hydro-Mooring-Control Simulation

Based on our in-house simulation code for HAWT [36,40], as well as the above algorithms for VAWT performance prediction, a coupled in-house numerical code, HeVAWT, is established in order to simulate the dynamic behaviors of the helical VAWT in the time domain. The basic procedure of this numerical tool is shown in Figure 5.
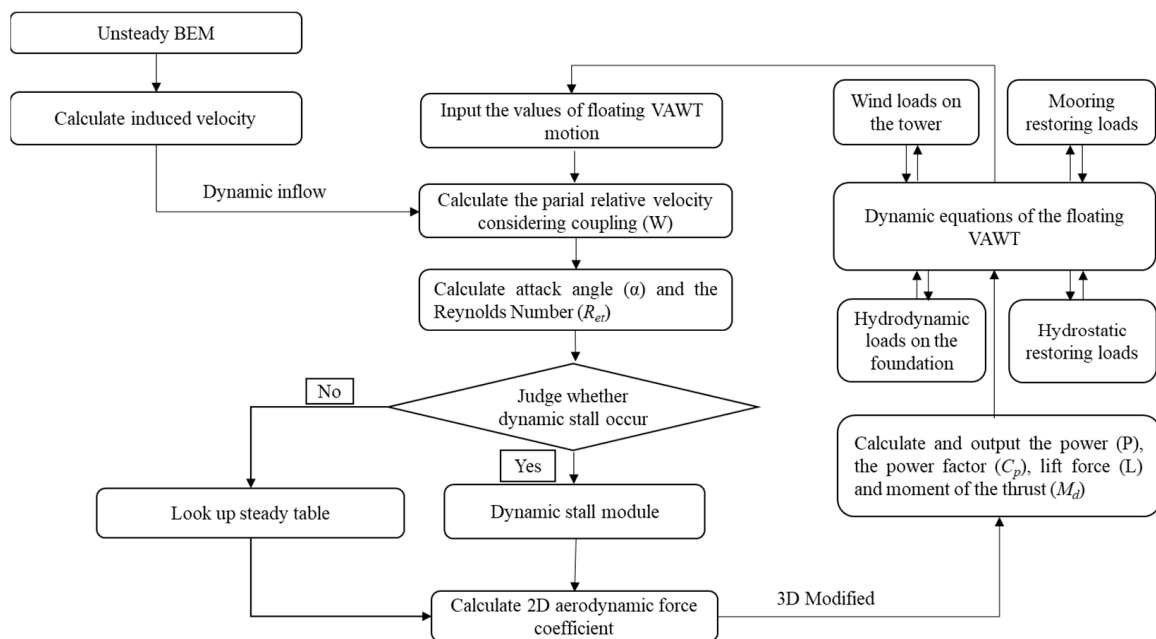

Figure 5. Flow chart of HeVAWT.

The governing equation of the VAWT, which is a multi-body system, is derived using Kane's dynamic equation, as the following shows:

$$F^{(p)} + F^{*(p)} + F^{(t)} + F^{*(t)} + F^{(b)} + F^{*(b)} = 0, \tag{10}$$

where the symbols *F* and *F** denote the generalized inertia and generalized active loads, respectively. The superscripts (*p*), (*t*), and (*b*) represent those loads calculated on the platform, tower, and blades, respectively. More derivations could be found in the dissertation [43]. After transferring the governing equation into the second-order time-state equation, we adopt the backward differentiation method (BDF) to solve the dynamic equation. By integrating the results with time, the dynamic performance of the VAWT could be achieved in the time domain.

4. Results and Discussion

In this section, we conduct several simulations to investigate the dynamic response of the helical VAWT according to the coupled simulation tool. To be specific, the controlling strategy is firstly described. This is followed by the simulations under the wind-only cases, and the influence on the start-up effect is discussed. Finally, four different levels of wind–wave scenarios are adopted to perform the time-domain simulations. The statistical

results of the dynamic responses, including aerodynamic performance, buoy motion, and mooring tension, are further analyzed and compared.

### 4.1. Controlling Strategy Considering the Output Power

Based on the aerodynamic algorithm proposed in Section 3.1, the output power performance of the VAWT is calculated under different wind speeds and rotor speeds. The grid points in Figure 6a show the power under the cases when the wind speed is lower than the rated, while those in Figure 6b represent the power under the over-rated wind speed cases.

(**a**)   (**b**)
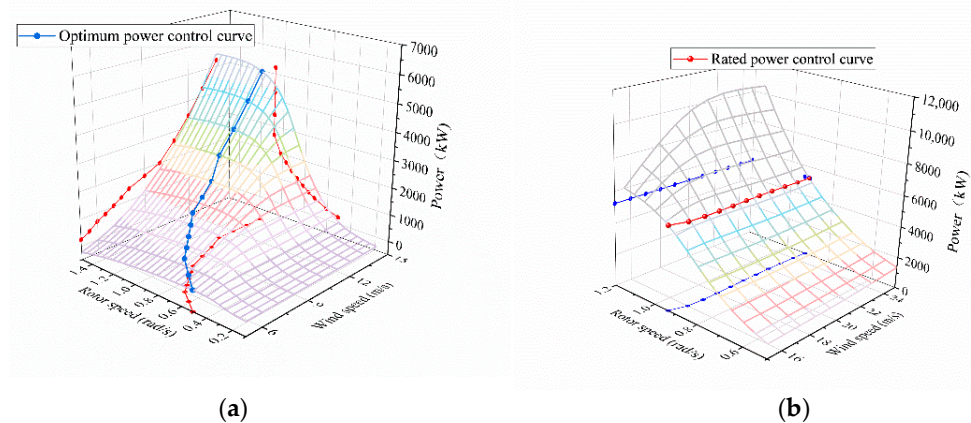
Figure 6. Output power via different wind speeds and rotor speeds. (**a**) Vw = 5–15 m/s; (**b**) Vw = 16–25 m/s.

Among those cases in Figure 6a, the aim of rotor speed is to search for the maximum output power. This part could be divided into two regions. When the rotor starts and its speed is lower than the rated (namely Region I), the maximum power point tracking (MPPT) algorithm is adopted to achieve the best tip speed ratio (TSR). In Region I, the output power has a cubic relationship with the rotor speed. On the other hand, when the rotor speed exceeds the rated and the wind speed is still lower than its corresponding rated speed (namely Region II), the rotor speed will be maintained at the rated level in order to avoid the large oscillating aerodynamic loads caused by the torque adjustment. When the wind speed keeps increasing over the rated in Figure 6b (namely Region III), the control target changes to keep the output power at the rated value (for example, 5.3 MW in the present study). Hereby, the rotor speed will be slowed down in order to reduce the aerodynamic torque and thrust, to ensure the structural safety.

According to these simulations, the targeted rotor speed via different wind speeds could be determined as Figure 7 shows. On the other hand, it should be noted that the aerodynamic torque depends on both transient wind speed and rotor speed; the accurate change rates of the rotor speed, U and L in Equation (5), cannot be determined. Herby, the upper bound U_{max} and lower bound L_{min} are calculated based on the average wind speed and its corresponding rotor speed, see Table 4. Another issue that should be pointed out is that the speed-up torque provided by the wind turbine remains at a low degree, and the lower bound has a significant influence on the controlling effect. Therefore, we assume that the absolute value of the decreasing rate is lower than that of the increasing rate, to ensure that the brake ability does not exceed the acceleration ability. Therefore, the sudden reduction in the rotor speed could be avoided.
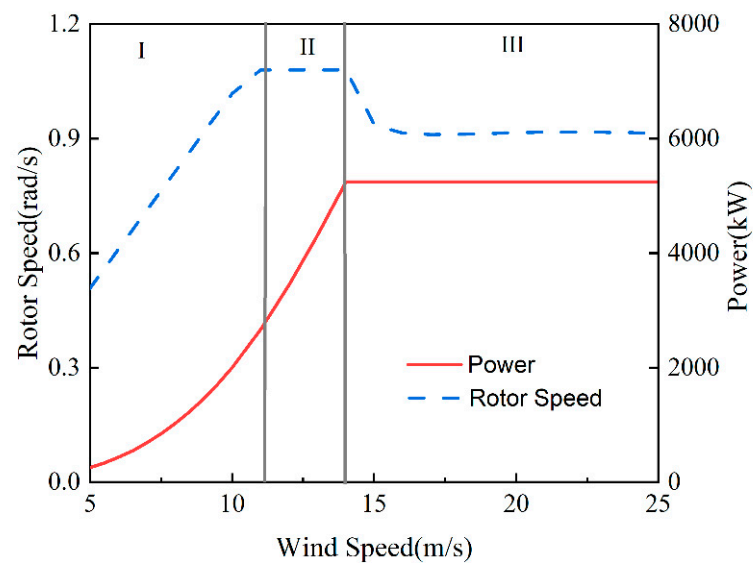
Figure 7. Rotor speed target and its corresponding output power via different wind speeds.

Table 4. Upper and lower bounds of the rotor speed changing rate.

Wind Speed (m/s)	L_{min}	U_{max}
5	−0.0035	0.0002
6	−0.0034	0.0003
7	−0.0033	0.0004
8	−0.0032	0.0005
9	−0.0030	0.0007
10	−0.0029	0.0008
11	−0.0026	0.0011
12	−0.0023	0.0014
13	−0.0020	0.0017
14	−0.0016	0.0021
15	−0.0013	0.0024
16	−0.0012	0.0025
17	−0.0012	0.0025
18	−0.0012	0.0025
19	−0.0012	0.0025
20	−0.0012	0.0024
21	−0.0012	0.0024
22	−0.0013	0.0024
23	−0.0012	0.0024
24	−0.0012	0.0024
25	−0.0012	0.0025

4.2. Start-Up Effect under Wind-Only Cases

When we switch on a wind turbine under the mild sea scenario, the transient loads may influence the structural responses, and, in some particular cases, the sudden start-up effect could lead to damage or safety issues. Hereby, the controller could be adopted to weaken this negative effect. In this subsection, we chose a wind-only sea state to perform the simulation. The average wind speed is 14 m/s, and its time history is displayed in Figure 8. Specifically, the IEC-Kaimal spectrum is adopted here and in the following simulations to generate the inflow wind. A 500 s simulation is performed, and the wind turbine is switched on at t = 50 s.
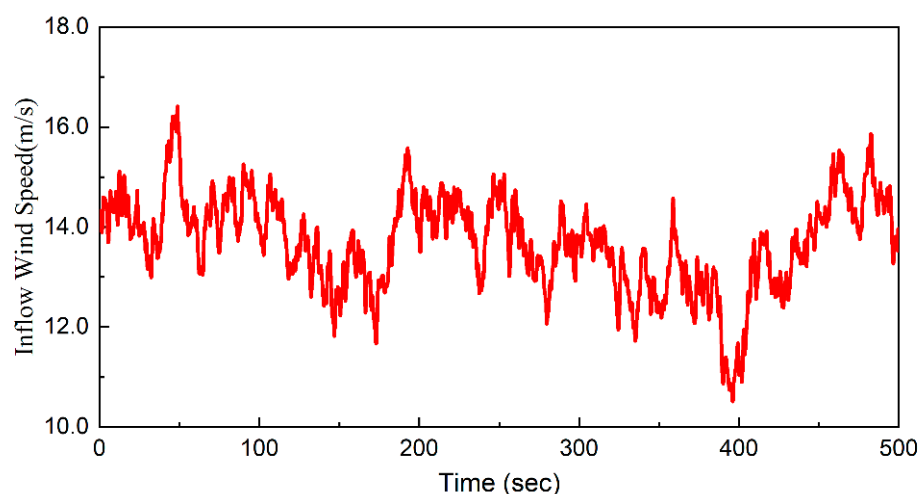
Figure 8. Time histories of wind speed.

Two different cases are adopted. One is the actual case and the other is the ideal case. Specifically, in the ideal case, the adjustment moment provided by the controller is assumed unlimited, so the rotor speed could suddenly reach the target value. In other words, the PID-based diagram in Figure 4 is the only controlling strategy, and the limitation of adjustment moment is not included in this case. On the other hand, however, the adjustment moment cannot reach the maximum suddenly. In the actual case, we set the extreme controller adjustment moment as 4.47×10^5 N·m, according to the nacelle ability, and the change rate of the moment is milder. The time histories of adjustment moment and rotor speed are displayed in Figure 8. The result shows that both the rotor speed and the adjustment moment after the start-up effect faded agree well with each case. The robustness of the controller strategy could be derived.

However, the start-up effects among both cases are distinguishable in the time histories. According to the results in Figure 9a, we could observe the jumping off effect from the adjustment moment curve under the ideal case. The extreme value suddenly changed from 0 to 5.576×10^6 N·m, and it quickly increased to 0 in 25 s. Comparing with the rotor speed in Figure 9b, the rotor speed also reached the target in this period. Apart from the possibility of this extremely large changing rate, this shocking moment could also damage the electronic system as well as the structural system. Therefore, the limitation of the adjustment moment is essential in the controller. After taking this parameter into consideration, the rotor speed was linearly raised in an even longer period of about 150 s, but the snap shock caused by the unreasonable large moment did not occur and the rotor could relent to start using the controller.

The time histories of output power are drawn in Figure 9c. Like the results of rotor speed, the final output power under both cases becomes converged. It can be also seen that the power rapidly increased to the rated level under the unlimited adjustment moment case. Particularly, at the initial start time of t = 50 s, the power even becomes negative under the ideal case. It means that the VAWT can be started only if consuming some external input energy. In the other actual case with limited adjustment moment, the power during the start-up stage monotone increased to the rated power. From this aspect, we found that the controlling efficiency would be overestimated if the limitation is not included. Moreover, it should be pointed out that some "overshooting" power exists which exceeds the rated power during the start-up duration. This is the general phenomenon for the VAWTs. Compared with the straight-blade-type VAWTs, the output power oscillations of the helical-blade ones are much lower. However, the controlling strategy will be further improved in the following study.

It is widely recognized that the aerodynamic loads will also affect the supporting platform motion; we hereby display the surge and yaw motions of the buoy as representative (see Figure 10). The surge motion is induced by the thrust loads on the rotor, while

the yaw motion is excited by the aerodynamic torque. According to the time histories in Figure 10, we can obviously find that the large oscillations in both surge and yaw will be excited. Specifically, the extreme surge amplitude exceeds 10 m and the yaw angle is almost 5 degrees. Although this transient large motion will be slowly reduced after about three cycles, it will undoubtedly increase the risks on the system safety. On the other hand, if the extreme adjustment moment is confined in a limited range, the overshooting displacement would be removed and it could smoothly move to its new equilibrium position. In other words, the system robustness could be confirmed and it will erase the negative influence on the structure damage on wind turbines, mooring lines, or even floaters.
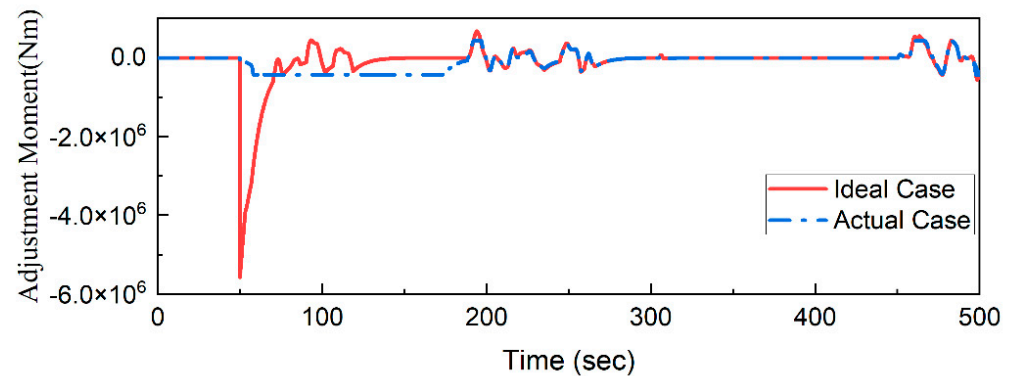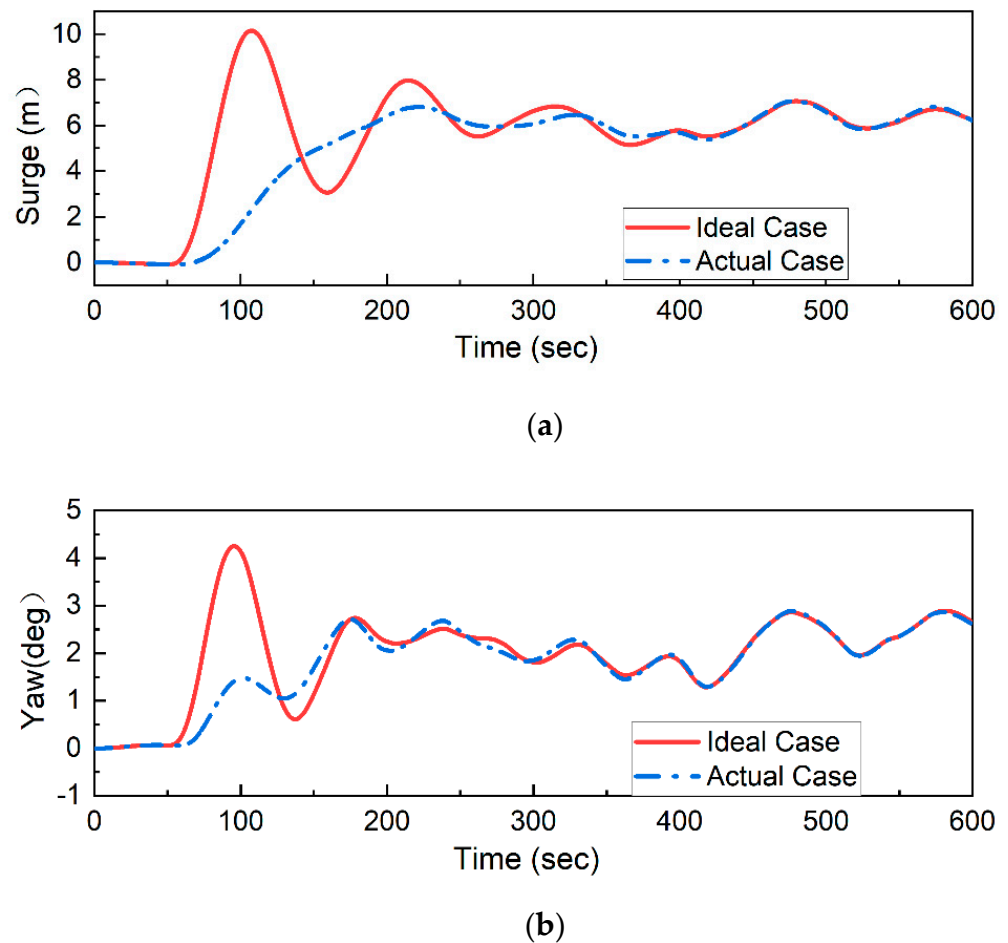

(**a**)
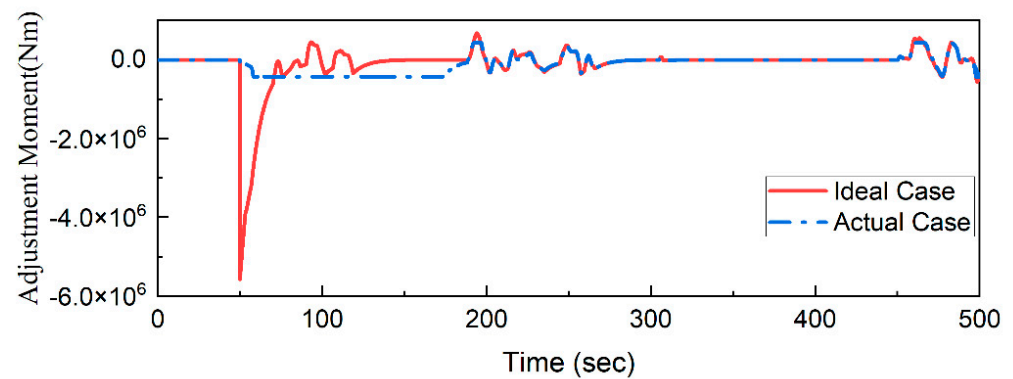
(**b**)
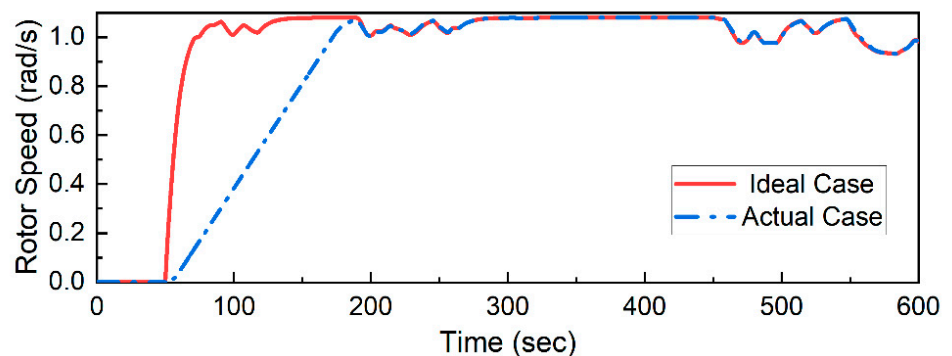
(**c**)

Figure 9. Wind turbine performance via different controlling strategies. (**a**) Adjustment moment; (**b**) Rotor speed; (**c**) output power.

(**a**)

(**b**)

Figure 10. Buoy motion via different controlling strategies. (**a**) Surge; (**b**) Yaw.

*4.3. Controlling Effect Validation Via Different Wind Speeds*

In order to validate the effectiveness of the controller, we further conduct a series of time-domain simulations under nine different wind speeds, in the range from cut-in speed to cut-off speed. Both steady wind and turbulence wind cases are adopted, taking the average wind speed of 14 m/s as an example, Figure 11 shows the time histories of the aerodynamic performance under both steady and turbulence wind cases. It can be seen that the wind turbine could operate stably after the start-up effect fades.

By collecting the stable period of output power and thrust (a duration of 6000 s after the start-up oscillation), their corresponding average values via different wind speed cases are presented Figure 12. It can be seen that under both steady wind and turbulence wind, the average power and thrust highly agree with the reference value. Hereby, the rotor speed tracking feature could be validated, which means that the controller could rapidly reflect to the inflow wind changes, and the rotor speed could be adjusted in order to maintain the aerodynamic performance of the VAWT at the target.
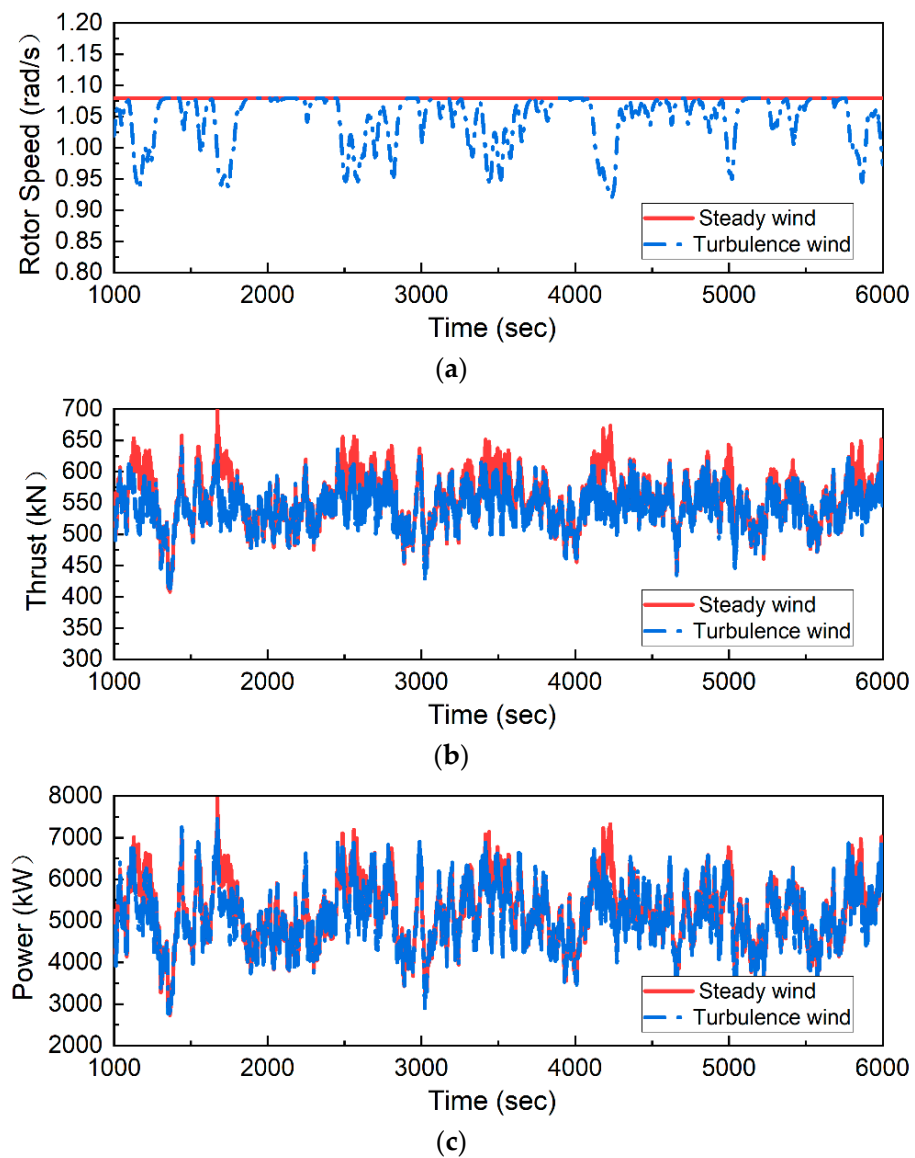
Figure 11. Aerodynamic performance of the case when the average wind speed is 14 m/s. (**a**) Rotor speed; (**b**) Thrust; (**c**) Output power.
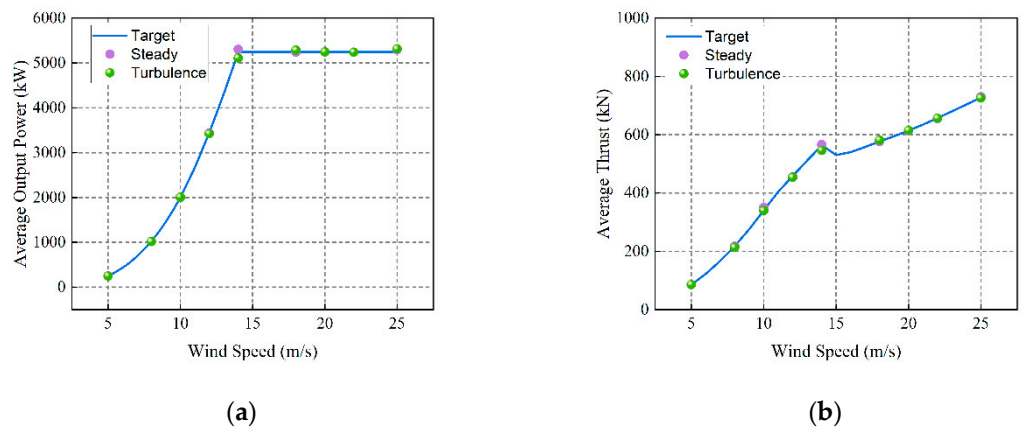
Figure 12. Aerodynamic performance of the VAWT under different wind speeds. (**a**) Output power; (**b**) Thrust.

4.4. VAWT Dynamic Responses under Wind–Wave Cases

The floating VAWT is operated under both wind and wave conditions, so it is important to examine the dynamic behaviors under these complicated sea scenarios, especially to make sure that the aerodynamic performance can avoid influence from the buoy motion. In this section, four different load cases are defined, and the corresponding wind-only cases are also adopted to be simulated for comparison, as Table 5 shows. Specifically, the wind speed corresponding to the equator plane (at the middle of the blades) is adopted in the following simulations. Three different kinds of responses, which are the rotor aerodynamic performance, buoy motions, and mooring loads, are chosen to be analyzed. In each simulation, a separate 3 h calculation is performed and the stable results are used for the statistical analysis.

Table 5. Load cases definition.

Load Case	Significant Wave Height (m)	Peaked Period (s)	Average Wind Speed (IEC-Kaimal) (m/s)
C1	2.88	9.98	10.00
C1.0	—	—	10.00
C2	3.62	10.29	14.00
C2.0	—	—	22.00
C3	4.44	10.66	18.00
C3.0	—	—	14.00
C4	5.32	11.06	22.00
C4.0	—	—	22.00

Figure 13 shows the box diagrams of the aerodynamic performance including thrust (Figure 13a), output power (Figure 13b), and the adjustment moment (Figure 13c), respectively. According to the results of thrust and output power, we could find that the difference between the extreme values of the thrust is amplified by the wave loads. The maximum difference among these four cases is 11.62%. With the wind speed and wave height increasing, the standard derivation of the thrust remains at the similar level. In other words, the controller could effectively reduce the large oscillations of the aerodynamic loads. On the other hand, based on the results in Figure 13b, the fluctuations under the rated sea state (C2) are the largest. To be specific, the ratio of max fluctuation to average value of the output power is 6.98%, which is lower than the 10% required by the grid connection.
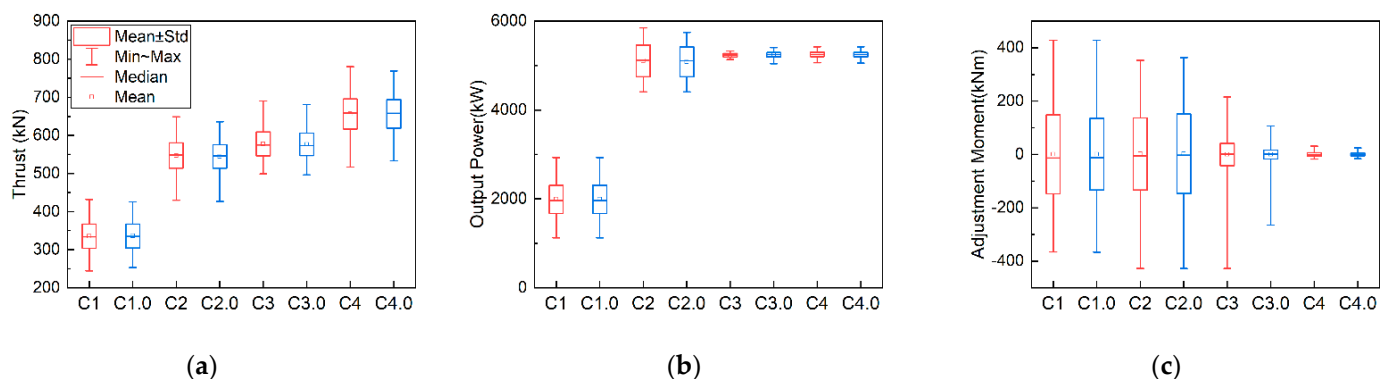

Figure 13. Aerodynamic performance under different wind–wave sea scenarios. (**a**) Thrust; (**b**) Output power; (**c**) Adjustment moment.

Moreover, according to the statistical results in Figure 13c, it could be observed that average adjustment moments are almost the same among different cases, although the wind speed is increasing. In other words, the controller is effective under the wind–wave cases. On the other hand, the extreme moments are almost the same between the wind-

only and wind–wave cases under the same wind speed. It means that the buoy-motion-induced relative wind speed cannot increase the adjustment moment, so the moment limitation works to avoid the overshooting. Another interesting phenomenon is that the adjustment moment in the highest load cases (C4 and C4.0) oscillates the least. It illustrates that the controller could effectively ensure the wind turbine stably operating under the severe scenarios.

Figure 14 shows the representative buoy motion under the load cases. On one hand, according to the surge results in Figure 14a, we see that the equilibrium position becomes farther away from the initial position with the larger wind speed. This is a similar trend as the mean aerodynamic thrust on the rotor, so it could be derived that the average surge position is highly dependent on the thrust. However, due to the wave drift load, the mean surge position could be further pushed away under the wind–wave cases. Another difference between the wind–wave cases and wind-only cases is that the surge oscillations are excited by the wave, especially under the stronger wave cases. For example, we could observe that surge fluctuations caused by waves under the extreme sea state are amplified by 200% between C4 and C4.0. However, the oscillations of the aerodynamic thrust and output power only increased by 4.7% and 1.0%, respectively, according to Figure 13a,b. This phenomenon shows that the control system could effectively maintain the stability under the extreme operational sea states.
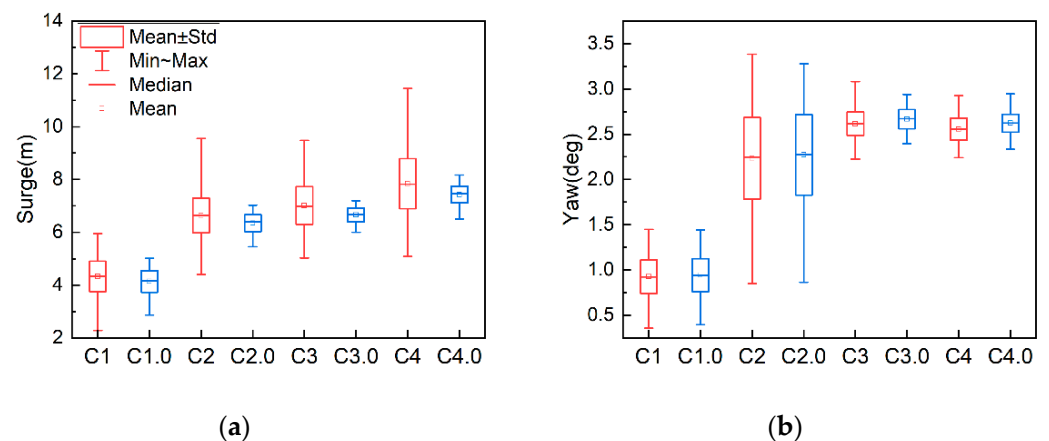
Figure 14. Buoy motion under different wind–wave sea scenarios. (**a**) Surge; (**b**) Yaw.

On the other hand, according to the yaw results in Figure 14b, we find that the average yaw angle increases with the wind speed, and it remains almost the same under the severe sea states (C3 and C4). This trend is similar to that of output power performance, to some degree. From this aspect, it could be concluded that the yaw motion is influenced by the aerodynamic torque on the rotor. Moreover, by comparing the results between wind-only and wind–wave cases, we see that the wave load has little effect under lower wind speed cases (C1 and C2), but the larger oscillations could be observed when the wind speed exceeds the rated. The phenomenon might be caused by the following factors. One is the slightly larger adjustment moment in order to keep the target rotor speed tracking; the other is the wave moments on the buoy becoming larger when the relative incident wave direction is changed by the average yaw angle. The mooring statistical results are displayed in Figure 15. Due to the symmetric configuration, the tensions of Lines 1 and 2 are chosen to be investigated. According to the results, the tension in Line 1 becomes larger with the increasing wind speed. Both average tension and the maximum tension under the wind–wave case are larger than those under wind-only case. On the contrary, the mean tension in Line 2 becomes lower under more severe cases, but the oscillations are still amplified. In fact, this is caused by the azimuth being located in the downwind direction. Therefore, the larger the drift distance under the higher wind speed, the slacker Line 2 will become.
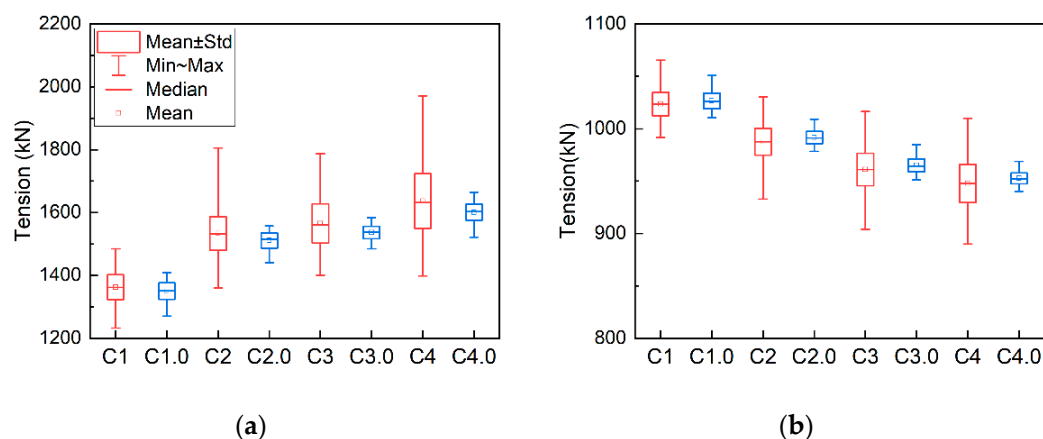
Figure 15. Line tensions under different wind–wave sea scenarios. (**a**) Line 1; (**b**) Line 2.

5. Conclusions

To investigate the dynamic responses of semi-submersible helical VAWT, an aero-hydro-mooring-control coupled dynamic model was established to perform the numerical simulations in the time domain. Particularly, due to coupled dynamic response caused by met ocean environmental loads, a suitable controller is essential for a better performance of the floating VAWT. To achieve this goal, an in-house coupled code was adopted, and it consisted of a 2D BEM model of VAWT, a 3D potential model of wave–body interaction of a semi-submersible buoy, a quasi-static catenary model of the mooring lines, and a PID-based controller model.

Taking the control efficiency and system robustness, a rotor speed controller was proposed to generate wind power smoothly. After the low-pass filter of the wind speed, the corresponding rotor speed was set as the target. By restricting the changing rate in a certain range, the over-estimated loads were avoided under the high wind speed cases, while the rapid adjustment on the rotor speed can also be achieved under the low wind speed scenarios. Based on the optimized floating VAWT, the dynamic behaviors under both wind-only and wind–wave cases were simulated. According to the investigation on the start-up effect, the VAWT could be switched on smoothly and the output power can be gradually increased to the rated power. Hereby, with the help of the controller system, it could guarantee safety of the VAWT structure and mooring lines. Therefore, it is necessary to take the adjustment moment into consideration, in order to accurate evaluate the effect of the controller during the start-up stage. Moreover, the average power and thrust could be retained at the rated level after the start-up effect is erased.

According to the results of wind–wave scenarios, it could be derived that the wave load could increase the oscillations of the supporting platform. By drawing the control system into the simulation, the aerodynamic thrust and output power of the helical VAWT are seldom influenced by the buoy motions and wave loads. Specifically, the surge fluctuations caused by waves under the extreme sea state are amplified by 200% compared to those under the similar-level wind-only case. However, the oscillations of the aerodynamic thrust and output power only increased by 4.7% and 1.0%, respectively. In other words, the effectiveness of the controller is significant under the severe sea state.

It is necessary to point out that the results are based on the numerical simulations. In the following work, a model test will be conducted to validate the controller as well as the coupled numerical codes. Furthermore, CFD and a better experiment design may also be of great importance.

On the other hand, as the blade pitch control cannot be adopted for the helical blade, the PID-based controller strategy cannot maintain the stable output power and aerodynamic loads on the blades, especially under the high wind speed cases. This may lead to the fatigue issue on the blades. With the developments of the piezoelectric materials, intelligent

blades could be manufactured in order to release the fatigue damage and make the output power more robust.

Another potential issue is the higher order wave load. When the water depth exceeds 200 m, the QTF-based second-order wave loads and Newman-approximation-based wave loads can be converged. Taking the simulation cost into consideration, it is a better way to adopt the Newman approximation in future research.

References

1. GWEC. *Global Offshore Wind Report 2020*; GWEC (Global Wind Energy Council): Brussels, Belgium, 2020.
2. Ren, Y.; Venugopal, V.; Shi, W. Dynamic analysis of a multi-column TLP floating offshore wind turbine with tendon failure scenarios. *Ocean Eng.* **2022**, *245*, 110472. [CrossRef]
3. Kumar, R.; Raahemifar, K.; Fung, A.S. A critical review of vertical axis wind turbines for urban applications. *Renew. Sustain. Energy Rev.* **2018**, *89*, 281–291. [CrossRef]
4. Hand, B.; Kelly, G.; Cashman, A. Numerical simulation of a vertical axis wind turbine airfoil experiencing dynamic stall at high Reynolds numbers. *Comput. Fluids* **2017**, *149*, 12–30. [CrossRef]
5. Hand, B.; Cashman, A.; Kelly, G. An aerodynamic modelling methodology for an offshore floating vertical axis wind turbine. In Proceedings of the 2015 International Conference on Renewable Energy Research and Applications (ICRERA), Palermo, Italy, 22–25 November 2015; pp. 273–277.
6. Liu, L.; Guo, Y.; Zhao, H.; Tang, Y. Motions of a 5 MW floating VAWT evaluated by numerical simulations and model tests. *Ocean Eng.* **2017**, *144*, 21–34. [CrossRef]
7. Islam, M.R.; Mekhilef, S.; Saidur, R. Progress and recent trends of wind energy technology. *Renew. Sustain. Energy Rev.* **2013**, *21*, 456–468. [CrossRef]
8. Apelfröjd, S.; Eriksson, S.; Bernhoff, H. A review of research on large scale modern vertical axis wind turbines at Uppsala University. *Energies* **2016**, *9*, 570. [CrossRef]
9. Hand, B.; Cashman, A. A review on the historical development of the lift-type vertical axis wind turbine: From onshore to offshore floating application. *Sustain. Energy Technol. Assess.* **2020**, *38*, 100646. [CrossRef]
10. Santamaría, L.; Oro, J.M.F.; Díaz, K.M.A.; Meana-Fernández, A.; Pereiras, B.; Velarde-Suárez, S. Novel methodology for performance characterization of vertical axis wind turbines (VAWT) prototypes through active driving mode. *Energy Convers. Manag.* **2022**, *258*, 115530. [CrossRef]
11. Zhu, X.; Guo, Z.; Zhang, Y.; Song, X.; Cai, C.; Kamada, Y.; Maeda, T. Numerical study of aerodynamic characteristics on a straight-bladed vertical axis wind turbine with bionic blades. *Energy* **2022**, *239*, 122453. [CrossRef]
12. Tjiu, W.; Marnoto, T.; Mat, S.; Ruslan, M.H.; Sopian, K. Darrieus vertical axis wind turbine for power generation I: Assessment of Darrieus VAWT configurations. *Renew. Energy* **2015**, *75*, 50–67. [CrossRef]
13. Tjiu, W.; Marnoto, T.; Mat, S.; Ruslan, M.H.; Sopian, K. Darrieus vertical axis wind turbine for power generation II: Challenges in HAWT and the opportunity of multi-megawatt Darrieus VAWT development. *Renew. Energy* **2015**, *75*, 560–571. [CrossRef]
14. Deng, W.; Liu, L.; Guo, Y.; Li, H. Effect of helical twist angle on the aerodynamic performance and blade dynamic characteristics of floating vertical axis wind turbines. *Mar. Struct.* **2022**, *83*, 103172. [CrossRef]
15. Deng, W.; Liu, L.; Li, Y.; Zhang, R.; Li, H. Slack coupled modeling method and dynamic analysis on floating vertical axis wind turbine with helical blades. *Ocean Eng.* **2022**, *246*, 110616. [CrossRef]

16. Wang, K.; Hansen, M.O.L.; Moan, T. Model improvements for evaluating the effect of tower tilting on the aerodynamics of a vertical axis wind turbine. *Wind Energy* **2015**, *18*, 91–110. [CrossRef]

17. Wang, K.; Hansen, M.O.L.; Moan, T. Dynamic analysis of a floating vertical axis wind turbine under emergency shutdown using hydrodynamic brake. *Energy Procedia* **2014**, *53*, 56–69. [CrossRef]

18. Cheng, Z.; Madsen, H.A.; Gao, Z.; Moan, T. Effect of the number of blades on the dynamics of floating straight-bladed vertical axis wind turbines. *Renew. Energy* **2017**, *101*, 1285–1298. [CrossRef]

19. Cheng, Z.; Madsen, H.A.; Chai, W.; Gao, Z.; Moan, T. A comparison of extreme structural responses and fatigue damage of semi-submersible type floating horizontal and vertical axis wind turbines. *Renew. Energy* **2017**, *108*, 207–219. [CrossRef]

20. Collu, M.; Borg, M.; Shires, A.; Brennan, F.P. FloVAWT: Progress on the development of a coupled model of dynamics for floating offshore vertical axis wind turbines. In Proceedings of the International Conference on Offshore Mechanics and Arctic Engineering, Nantes, France, 9–15 June 2013; Volume 55423, p. V008T09A045.

21. Borg, M.; Collu, M. Frequency-domain characteristics of aerodynamic loads of offshore floating vertical axis wind turbines. *Appl. Energy* **2015**, *155*, 629–636. [CrossRef]

22. Borg, M.; Collu, M. A comparison on the dynamics of a floating vertical axis wind turbine on three different floating support structures. *Energy Procedia* **2014**, *53*, 268–279. [CrossRef]

23. Owens, B.; Hurtado, J.E.; Paquette, J.A.; Griffith, D.T.; Barone, M.F. Aeroelastic modeling of large off-shore vertical-axis wind turbines: Development of the offshore wind energy simulation toolkit. In Proceedings of the 54th AIAA/ASME/ASCE/AHS/ASC Structures 2013, Structural Dynamics, and Materials Conference, Boston, MA, USA, 8–11 April 2013; p. 1552.

24. Owens, B.C.; Griffith, D.T.; Hurtado, J.E. Modal dynamics and stability of large multi-megawatt deepwater offshore vertical-axis wind turbines: Initial support structure and rotor design impact studies. In Proceedings of the 32nd ASME Wind Energy Symposium, National Harbor, MD, USA, 13–17 January 2014; p. 0518.

25. Vita, L.; Paulsen, U.S.; Madsen, H.A.; Nielsen, P.H.; Berthelsen, P.A.; Carstensen, S. Design and aero-elastic simulation of a 5 MW floating vertical axis wind turbine. In Proceedings of the International Conference on Offshore Mechanics and Arctic Engineering, Rio de Janeiro, Brazil, 1–6 July 2012; Volume 44946, pp. 383–392.

26. Deng, W.; Yu, Y.; Liu, L.; Guo, Y.; Zhao, H. Research on the dynamical responses of H-type floating VAWT considering the rigid-flexible coupling effect. *J. Sound Vib.* **2020**, *469*, 115162. [CrossRef]

27. Gao, J.; Griffith, D.T.; Sakib, M.S.; Boo, S.Y. A semi-coupled aero-servo-hydro numerical model for floating vertical axis wind turbines operating on TLPs. *Renew. Energy* **2022**, *181*, 692–713. [CrossRef]

28. Tan, L.; Ikoma, T.; Aida, Y.; Masuda, K. Mean Wave Drift Forces on a Barge-Type Floating Wind Turbine Platform with Moonpools. *J. Mar. Sci. Eng.* **2021**, *9*, 709. [CrossRef]

29. Ikoma, T.; Tan, L.; Moritsu, S.; Aida, Y.; Masuda, K. Motion characteristics of a barge-type floating vertical-axis wind turbine with moonpools. *Ocean Eng.* **2021**, *230*, 109006. [CrossRef]

30. Zheng, X.; Zheng, H.; Lei, Y.; Chen, H. Nonlinear stochastic responses of a newly developed floating wind-solar-aquaculture system. *Ocean Eng.* **2021**, *241*, 110055. [CrossRef]

31. Carstensen, S. *Future Deep Sea Wind Turbine Technologies*; DTU Wind Energy: Roskilde, Denmark, 2012.

32. Svendsen, H.G.; Merz, K.O.; Endegnanew, A.G. Control of floating vertical axis wind turbine. In Proceedings of the European Wind Energy Conference and Exhibition, Copenhagen, Denmark, 16–19 April 2012.

33. Merz, K.O.; Svendsen, H.G. A control algorithm for the deepwind floating vertical-axis wind turbine. *J. Renew. Sustain. Energy* **2013**, *5*, 063136. [CrossRef]

34. Cheng, Z.; Wang, K.; Gao, Z.; Moan, T. A comparative study on dynamic responses of spar-type floating horizontal and vertical axis wind turbines. *Wind. Energy* **2017**, *20*, 305–323. [CrossRef]

35. Guo, Y.; Liu, L.Q.; Lv, W.D.; Tang, Y.G. The aerodynamic analysis of Helical-type VAWT with semi empirical and CFD method. In Proceedings of the ASME 2019 38th International Conference on Ocean, Offshore and Arctic Engineering, Glasgow, UK, 9–14 June 2019.

36. Robertson, A.; Jonkman, J.; Masciola, M.; Song, H.; Goupee, A.; Coulling, A.; Luan, C. *Definition of the Semisubmersible Floating System for Phase II of OC4[R] 2014*; National Renewable Energy Laboratory (NREL): Golden, CO, USA, 2014.

37. Li, Y.; Zhu, Q.; Liu, L.; Tang, Y. Transient response of a SPAR-type floating offshore wind turbine with fractured mooring lines. *Renew. Energy* **2018**, *122*, 576–588. [CrossRef]

38. Marini, M.; Gazzano, R.; Satta, A. Semi-Empirical Methods for the Analysis of Vertical Axis Wind Turbines with Helical Blades. In Proceedings of the Turbo Expo: Power for Land, Sea, and Air, Glasgow, UK, 14–18 June 2010; Volume 44007, pp. 883–890.

39. Liu, L.; Guo, Y.; Jin, W.; Yuan, R. Motion Performances of a 5 MW VAWT Supported by Spar Floating Foundation With Heave Plates. In Proceedings of the ASME 2017 36th International Conference on Ocean, Offshore and Arctic Engineering, American Society of Mechanical Engineers, Trondheim, Norway, 25–30 June 2017; p. V010T09A086.

40. Salehyar, S.; Li, Y.; Zhu, Q. Fully-coupled time-domain simulations of the response of a floating wind turbine to non-periodic disturbances. *Renew. Energy* **2017**, *111*, 214–226. [CrossRef]

41. Qu, X.; Li, Y.; Tang, Y.; Hu, Z.; Zhang, P.; Yin, T. Dynamic response of spar-type floating offshore wind turbine in freak wave considering the wave-current interaction effect. *Appl. Ocean Res.* **2020**, *100*, 102178. [CrossRef]

42. Li, Y.; Qu, X.; Liu, L.; Xie, P.; Yin, T.; Tang, Y. A Numerical Prediction on the Transient Response of a Spar-Type Floating Offshore Wind Turbine in Freak Waves. *J. Offshore Mech. Arct. Eng.* **2020**, *142*, 062004. [CrossRef]
43. Yuan, R. Rigid-Flexible Coupling Dynamic Simulation of Floating Vertical Wind Turbine System Based on Kane Method. Master's Thesis, Tianjin University, Tianjin, China, 2018. (In Chinese).